$LaAu_2$ and $CeAu_2$ surface alloys grown by reactive deposition on Au(111)

M. Ormaza,[1] L. Fernández,[2] M. Corso,[2] F. Schiller,[3] B. Xu,[4] M. Diakhate,[4] M. J. Verstraete,[4] and J. E. Ortega[1,2,3]
[1]*Universidad del País Vasco, Dpto. Física Aplicada I, E-20018 San Sebastián, Spain*
[2]*Donostia International Physics Center, Paseo Manuel Lardizabal 4, E-20018 San Sebastián, Spain*
[3]*Centro de Física de Materiales CSIC/UPV-EHU-Materials Physics Center, Manuel Lardizabal 5, E-20018 San Sebastián, Spain*
[4]*Université de Liège, Institut de Physique, allée du 6 août, numéro 17 Sart-Tilman B-4000 Liège, Belgium*

(Dated: June 4, 2013)

We report on the crystal structure and the electronic bands of $LaAu_2$ and $CeAu_2$ surface alloys grown by reactive deposition on Au(111). By Scanning Tunneling Microscopy we study the formation of different alloy phases as a function of growth temperature and lanthanide coverage. We determine the specific growth conditions to achieve monolayers and bilayers of $LaAu_2$ and $CeAu_2$ with high crystalline quality. Due to lattice mismatch with the underlying Au substrate, both $LaAu_2$ and $CeAu_2$ surface alloys exhibit long range moiré patterns, which can serve as templates for further nanostructure growth. By Angle Resolved Photoemission we map the two-dimensional band structure of these surface alloys, discussing the nature of the different spectral features in the light of first principles theory calculations.

INTRODUCTION

The ability to control and modify the structure and the electronic properties of surfaces is of key importance to develop technologically relevant materials. Surface alloying is a straightforward route to tune surface electronic states and geometric structure. From the electronic point of view, the tunable chemical composition of the surface layer is of great importance, e.g., to optimize catalytic processes [1], and in general to tailor exotic nanoscale electronic properties. Structurally, surface-confined alloying can be exploited, e.g., to tune moiré patterns and dislocation networks, which characterize many metal overlayer systems with lattice mismatch. Such periodically modulated surfaces have great potential as nanotemplates for self-organized growth of nanostructures [2–5].

The $GdAu_2$ alloy is a good example of a periodically-modulated metallic surface induced by alloying [2, 6, 7]. In fact, high temperature deposition of Gd on Au(111) gives rise to stable $GdAu_2$ mono and bilayers with a high crystalline quality that present long-range moiré patterns. This system has been shown to behave as a very effective nanoscale template for highly dense Co nanodot arrays [2]. The full structural and electronic characterization of both, monolayers and bilayers, demonstrates that such $GdAu_2$ surface alloy is actually a novel phase, with distinct layer stacking compared to the bulk $GdAu_2$ crystal [6]. Additionally, exotic magnetic properties are predicted, which may have strong influence on the magnetic anisotropy of Co nanodots that nucleate in the moiré lattice [8].

In this work we apply the same reactive growth procedure to lanthanum and cerium, on Au(111). These two elements are particularly attractive to investigate the role of the substrate in the magnetic properties of nanodot arrays. Compared to Gd, La and Ce have similar valence electronic states but different numbers of $4f$ electrons, i.e., those that determine the special magnetism of rare earths (RE) [9, 10]. La does not have $4f$ e^- and hence is not magnetic, whereas Ce possesses one $4f$ e^- and is known to behave magnetically in a very peculiar way [11–14]. We demonstrate that both La and Ce form surface-confined alloys on Au(111), in a similar way to $GdAu_2$ [7]. Among them, $LaAu_2$ and $CeAu_2$, which exhibit high crystal quality and a moiré structure, the latter of potential interest for magnetic nanodot growth. In the light of Angle Resolved Photoemission Spectroscopy (ARPES), Scanning Tunneling Microscopy (STM) experiments, and first principles theory we discuss the nature, the analogies and the differences in electronic states and structure among these three $REAu_2$ surface alloys.

EXPERIMENT AND THEORY DETAILS

Scanning Tunneling Microscopy (STM) experiments were performed in a VT-Omicron setup operating at 300 K. Angle resolved Photoemission Spectroscopy (ARPES) experiments were carried out at the PGM beam line of the Synchrotron Radiation Center (SRC) in Stoughton (Wisconsin). We used a hemispherical Scienta SES200 spectrometer with energy and angular resolution set to 25 meV and 0.2°, respectively and p-polarized light. La and Ce were deposited from e-beam evaporators at a base pressure below $p = 5 \cdot 10^{-9}$ mbar, and with the Au(111) single crystal sample held at different temperatures. The substrate temperature during the evaporation of La and Ce is crucial to optimize the homogeneity and extension of the moiré structure. Substrate temperatures used for evaporation varied around 780 K for La and between 650 K and 750 K for Ce. Below these temperatures the moiré is not well formed or other phases dominate, and above them, the RE metal fades away into the bulk or re-evaporates to vacuum. The optimal substrate temperature in each case was fixed in ARPES measurements, where we could track the evolution of the electronic structure as a function of the thickness by evaporating RE films as linear wedges. These could be accurately scanned thanks to the small size of the synchrotron beam ($100\,\mu m$).

Calculations for the surface alloys are carried out within the framework of density functional theory, using the ABINIT package [15]. We adopt the local density approximation and the projector augmented-wave method [16], with plane wave cut off energy of 20 Ha. The potentials of La, Ce and Au are constructed with 11, 12 and 11 valence electrons, and with cutoff radii of 3.02, 2.51 and 2.69 bohr, respectively. For each angular momentum channel two projectors are used. A $\sqrt{3} \times \sqrt{3}$ unit cell ($d_{\sqrt{3}\times\sqrt{3}}$ = 4.99 Å) is used for the alloy, with 7 layers of Au substrate and a minimum of 8.3 Å of vacuum between periodic slab images. Good convergence for the bulk Au states is achieved with the k-point sampling in the Brillouin zone on an unshifted 12×12 grid. To include the strong correlation of f electrons, the LDA+U method is used. The Hubbard parameters are U=8.0 eV and J=0.7 eV for La, and U=6.1 eV and J=0.7 eV for Ce [17]. The Ce calculations are performed with collinear spin polarization that allows the description of the magnetic states.

Three different surface structures have been considered for the alloy layers, one on-top (primitive hexagonal stacking $\cdots$ABCABCA**A**) and two hollow configurations (fcc $\cdots$ABCABCA**B** and hexagonal close packed $\cdots$ABCABCA**C**), relative to the atomic positions of the Au sublayer below the ML. After fixing the in-plane lattice constant to the theoretically relaxed Au bulk value, the structures have been optimized allowing the ML and two Au sublayers to relax, until the forces on atoms are less than 1×10^{-5} Ha/Bohr. The ground state is given by the fcc hollow configuration. In the La case the hcp hollow surface structure is slightly unfavorable, but the hexagonal on-top configuration is significantly higher than the ground state (583 meV for LaAu$_2$). For Ce the convergence of a clear magnetic state is more problematic, and the different layer orderings have not been fully resolved in energy. We have used the fcc hollow structure for CeAu$_2$ as well, to be consistent with the other RE. The moiré structure will yield different alloy alignments in different regions of the substrate, but we proceed using the most stable hollow structure as a reference. All three configurations yield ferromagnetic states for Ce, with magnetizations of about 1 μ_B that arise from the 4f electrons.

GROWTH OF LAAU$_2$ AND CEAU$_2$ SURFACE ALLOYS

Figures 1-3 show characteristic STM images taken after the high temperature deposition of La (Fig. 1) and Ce (Figs. 2-3) on Au(111) at different length scales. We observe a complete analogy with the case of GdAu$_2$ [7]. It is possible to tune the deposition parameters to obtain the pure LaAu$_2$ surface phase with its characteristic moiré pattern. In fact, homogeneous LaAu$_2$ moiré patterns with the highest crystal quality, and extending over the whole surface are achieved with the substrate held at 780K. The lattice periodicity of the moiré is (32±2) Å, as determined from the large scale view in Fig. 1 (a). The nearest neighbor distance (5.3±0.3) Å measured in the atomically-resolved image in panel Fig. 1 (b) corresponds to the size of

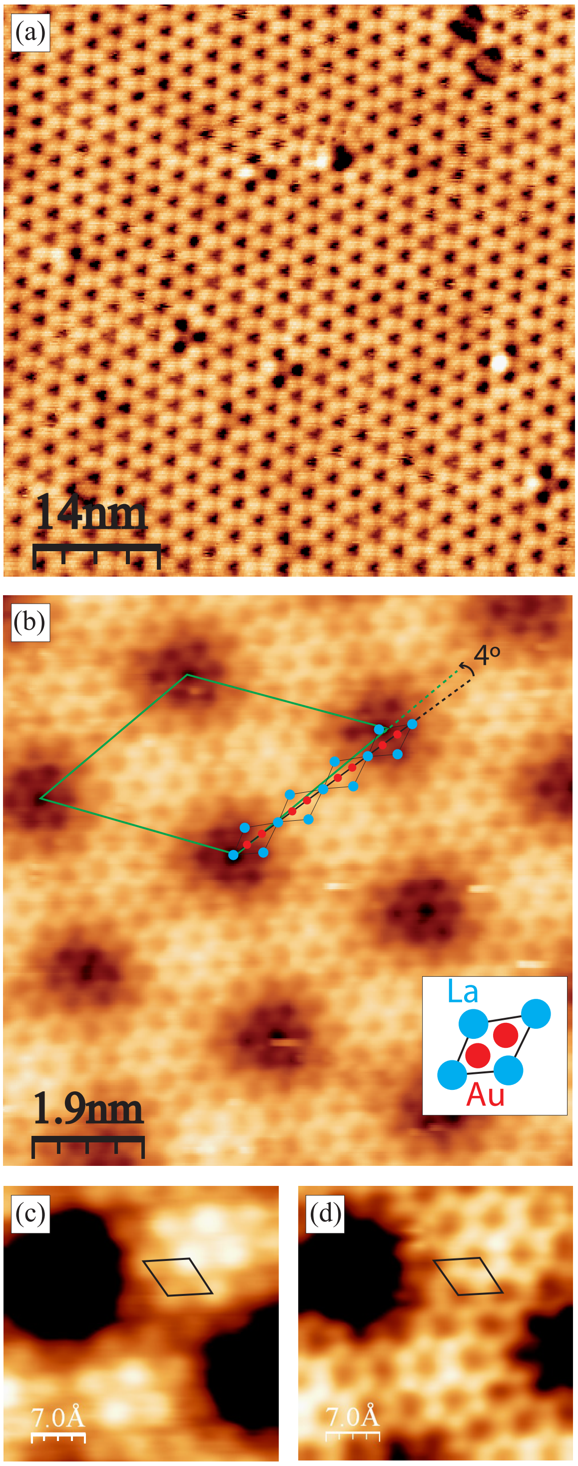

FIG. 1: STM images of the LaAu$_2$ surface alloy taken at different length scales. (a) At a large scale, the hexagonal moiré superstructure is characterized by slightly undulated rows of triangles, with punctual defects. As shown in (b), the wavy appearance of the moiré is linked to a variable misalignment of the atomic lattice with respect to the moiré structure, with a maximum of 4°, as shown in the overlaid drawing. The LaAu$_2$ unit cell is sketched in the inset. (c) and (d) Atomically resolved STM images of the LaAu$_2$ surface alloy revealing one protrusion (probably La) per unit cell in (c), and two protrusions (Au atoms) in a honeycomb arrangement in (d). Image parameters: (a-b) -2 V, 0.1 nA, (c) -2 V, 1 nA and (d) -2 V, 0.1 nA.

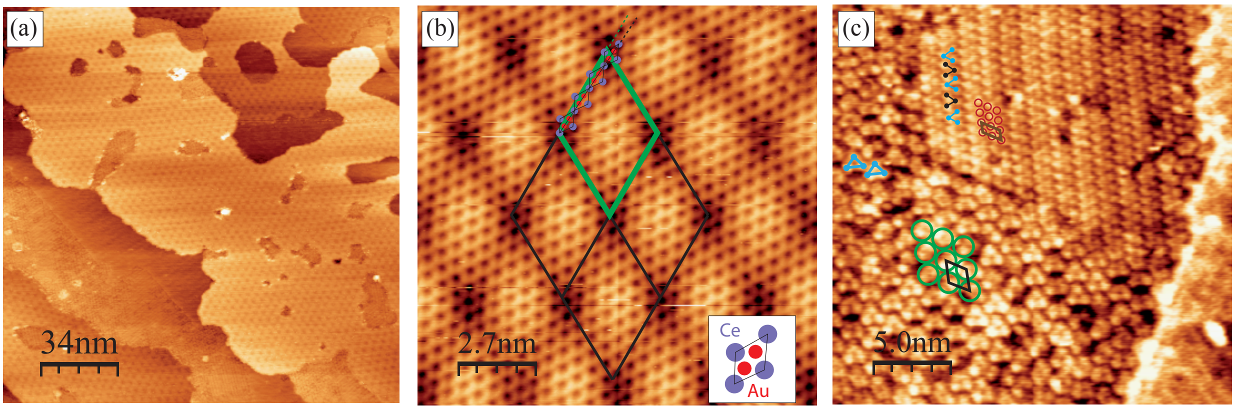

FIG. 2: (a) Large scale STM view obtained after reactive evaporation of 4 Å Ce on Au(111) at 750 K. Around 70% of the surface is covered by $CeAu_2$ moiré phase. The rest of the surface (30%) mainly consists of irregularly shaped areas filled with triangular clusters. (b) Atomically resolved STM images of the $CeAu_2$ moiré phase. The atomic structure is defined as a hexagonal lattice of holes. The inset shows the $CeAu_2$ unit cell. In the image, the large unit cell marks the moiré superstructure while the small hexagonal unit cell refers to the $CeAu_2$ atomic lattice; (c) Morphology of the Ce-Au alloy at triangular cluster areas away from the $CeAu_2$ moiré lattice. The three lobes that form a single cluster are arranged forming a triangle (in blue). Quasi-hexagonal and double chain structures of such clusters coexist. The small circles in green denote the quasi-hexagonal arrangement, where each circle represents a cluster. The surface unit cell is marked in black. The triangular clusters with double chain structure display an overall rectangular surface unit cell (in brown) that is represented by the small red circles. Each circle contains a single circular lobe. It is seen that each of the three lobes form well defined triangles that change alternatively their orientation to the right (black) or to the left (blue) along a single chain. Image parameters: (a) -1.5 V, 0.5 nA, (b) 0.05 V, 2 nA and (c) 1 V, 1 nA.

.

the unit cell of the $LaAu_2$ overlayer, which is depicted in the inset of panel (b). Figs. 1 (c) and (d) reveal a variable atomic contrast within the unit cell, which exclusively depends on the tunneling current (I_t), i.e., the tip sample distance. At bias voltages (U_b=-2 V), far from the Fermi level (E_F), and I_t=1 nA the unit cell is featured as a single protrusion, while for I_t=0.1 nA we clearly define a honeycomb arrangement. A straightforward interpretation assigns the protrusions to La atoms in the former image, and to the pair of Au atoms in the latter one.

As in $GdAu_2$, the moiré arises due to the superposition of the different $LaAu_2$ and Au(111) lattices. Both STM and Low Energy Electron Diffraction (LEED) measurements reveal that the $LaAu_2$ atomic lattice is rotated by 30° with respect to the Au(111) substrate. The La-Au in-plane distance d_{La-Au}= (3.1±0.2) Å deduced from Figs. 1 (b)-(d) is larger than the Au(111) substrate lattice constant (nominally, (2.8 ± 0.3) Å [7]), giving rise to a coincidence of the hexagonal (10.4×10.4) $LaAu_2$ lattice with the (11.4×11.4) Au(111) lattice, which explains the moiré. The $LaAu_2$ overlayer is thus incommesurate with respect to the Au(111) substrate, which is reflected by local deviations in the moiré periodicity. Random atom vacancies and defects, visible in Fig. 1 (a), are more frequent than in $GdAu_2$ and may be partly triggered by such lattice incommensurability. On the other hand, the hexagonal moiré lattice in Fig. 1 (b) appears rotated by $\sim$ 30° with respect to the $LaAu_2$ atomic lattice, in agreement with LEED measurements. In reality, the azimuthal misalignment of the moiré and the atomic lattices varies smoothly within $-4°$ to $4°$ across the surface. This variation explains the wavy aspect of the superlattice in large scale images, such as that of Fig. 1 (a), and reflects again the incommensurability of the $LaAu_2$ and Au(111) atomic lattices.

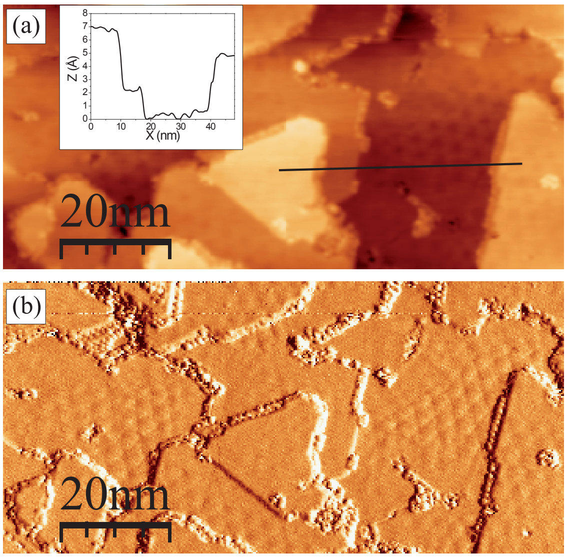

FIG. 3: STM pictures for >5Å Ce evaporated on Au(111) at 650 K. The growth conditions permit the nucleation of a pure $GdAu_2$ moiré phase, eliminating triangular clusters of Fig. 2 (c). However, the lower substrate temperature leads to a rougher morphology with coexisting monolayer and bilayer islands. (a) Topography and line profile. (b) Current image enhancing the moiré corrugation, which is attenuated in 2 ML thick islands with respect to the 1 ML structure.

The reactive growth of a pure $CeAu_2$ alloy with optimum morphology and crystallinity is more difficult than in the case of $LaAu_2$ or $GdAu_2$. The evaporation of Ce on Au(111) at temperatures between 650 K and 750 K gives rise to the formation of different reacted phases that coexist with the $CeAu_2$ moiré. The best results are obtained by holding the substrate temperature at 750 K and dosing the total amount of Ce to an equivalent 4 Å thickness. In this case, the $CeAu_2$ moiré phase homogeneously extends to about 70% of the surface, coexisting with (Ce-Au)-triangular clusters distributed in small areas. The characteristic morphology at a large scale is shown in Fig. 2 (a), whereas Fig. 2 (b) shows the atomically-resolved STM image of the $CeAu_2$ moiré phase. The latter exhibits a superperiodic unit cell with (33 ± 2) Å lattice constant, and a nearest neighbor distance of (5.4 ± 0.3) Å, which corresponds to the $CeAu_2$ surface unit cell dimensions. As in Fig. 1 (d) for $LaAu_2$, at these particular tunneling conditions the unit cell protrusions define the honeycomb-like structure expected for the Au atom sublattice. Similarly to Gd and La, the moiré pattern reflects the mismatch between the in-plane Ce-Au atomic distance (d_{Ce-Au}=(3.1±0.2) Å) in the alloy and the atomic distance in the Au(111) surface. In the same way as Gd and La, the $CeAu_2$ is 30° rotated with respect to the Au(111) plane. This results in a coincidence lattice of (10.6×10.6) $CeAu_2$ on top of a (11.6×11.6) Au(111), suggesting that the $CeAu_2$ overlayer is incommensurate with the Au(111) substrate, as in the case of La. The moiré pattern also exhibits an average 30° rotation with respect to the surface unit cell of $CeAu_2$, with a smoothly varying misalignment analogous to that of $LaAu_2$, as indicated in Fig. 2 (b).

Figure 2 (c) examines the (Ce-Au)-triangular clusters that coexist with the $CeAu_2$ moiré structure. The clusters are apparently formed by three spherical lobes arranged in a triangle-like geometry, and can be found forming hexagons (bottom part of the image) or double chains (top part of the image). Those arranged as double chains present an ordered phase with a rectangular surface unit cell of (17.2 Å×14.5 Å), while the hexagonal clusters lack long-range order. We can refer in this case to a quasi-hexagonal arrangement with a nearest neighbor distance around 14.5 Å. There are similarities between both structures, and it seems that the quasi-hexagonal phase is a precursor of the double chain. In the latter case the three lobes are ordered forming well defined, close-packed triangles that give place to chains, as marked in Fig. 2 (c).

The triangular cluster phase can be eliminated by lowering the substrate temperature to 650 K and increasing the Ce coverage above 5 Å. In such case, the $CeAu_2$ phase is the only one observed, but the surface becomes rougher, i.e., three-dimensional $CeAu_2$ islands develop on top of a $CeAu_2$ interface layer [Fig. 3]. The $CeAu_2$ islands exhibit both monolayer (ML) and bilayer (BL) heights, i.e., 2.2 Å and 4.5 Å, respectively. These values equal the interlayer distance of 2.2Å for $GdAu_2$, as determined by X-ray photoelectron diffraction [6]. The tunneling current image in Fig. 3 (b) shows the evolution of the moiré pattern with the number of layers. The moiré pattern on top of the islands becomes weaker and eventually disappears, as the interface stress is released [see Fig. 3 (b)]. On the other hand, a further reduction of the evaporation temperature down to 300 K, leads to another family of alloys with reduced Au content [18], as also observed in the case of Gd [7]. In this case, the $CeAu_2$ stoichiometry and its characteristic moiré can be recovered after post-annealing to 750 K, but its relative proportion with respect to other Ce-Au reacted phases is much lower than the 70% maximum obtained by direct growth at 750 K.

ELECTRONIC STATES

The 2D electronic band structure of $LaAu_2$ and $CeAu_2$ surface alloys are obtained by Angle Resolved Photoemission. ARPES experiments were performed on wedge-evaporated samples, which allow to accurately define 1 ML and 2 ML coverages. The 1 ML point in the wedge is determined by the complete quenching of the Shockley surface state of the Au(111) substrate, whereas the thickness beyond 1 ML is controlled with the Au $4f$ core-level intensity. However, due to the inherent difficulties of mimicking the STM growth conditions (temperature, flux) to obtain the purest $LaAu_2$ and $CeAu_2$ phases, a general consistency is sought with all, surface state and core-level intensity analysis, quartz microbalance reading, valence band spectral features (discussed below) and comparing with the already studied $GdAu_2$ alloy [7]. For the sake of comparison, $GdAu_2$ data are included in valence-band spectra in Figs 6 and 7.

Fig. 4 illustrates the transformation of Au $4f$ core-levels after $LaAu_2$ and $CeAu_2$ growth, presenting a completely analogous behavior compared to the synthesis of the $GdAu_2$ surface alloy [6, 7]. The spectrum spans the entire Au $4f$ core-level region, including the two spin-split components $4f^{5/2}$ and $4f^{7/2}$. Peaks labelled "2" and "4" correspond to the surface core-level shift of Au, whereas peaks "1" and "3" correspond to Au atoms in both the alloy and the bulk crystal. These cannot be resolved, although a smooth shift ΔE=70 meV (60 meV in Ce) to higher binding energies is observed from the pure bulk component to the alloy. As shown in the corresponding insets, the Au surface state goes to zero across the wedge at the same rate at which the alloy/bulk peak intensity increases and reaches its maximum. For La, the core-level intensity decreases for 2 ML, as expected from the attenuation effect of La atoms in thicker alloy films. For Ce, the bulk/alloy Au $4f$ signal remains constant beyond 1 ML, indicating that the second layer of $CeAu_2$ is not actually being formed, probably due to an excess annealing temperature.

Top pannels in Fig. 5 show the band structure measured along the $\overline{\Gamma K}$ symmetry direction [19] in $CeAu_2$ ML [panel (a)], and $LaAu_2$ ML [panel (b)] and bilayer [panel (c)]. The data correspond to the second derivative of the photoemission intensity, which allows to enhance band features over the intense steep background (see Fig. 7). For 1 ML, very similar A, B, C and C' bands are identified in both $CeAu_2$ and $LaAu_2$, which are also analogous to those found for $GdAu_2$ [6]. Band energies are listed in table I, for the whole family of alloys. Close to E_F, A band has an electron-like parabolic dispersion

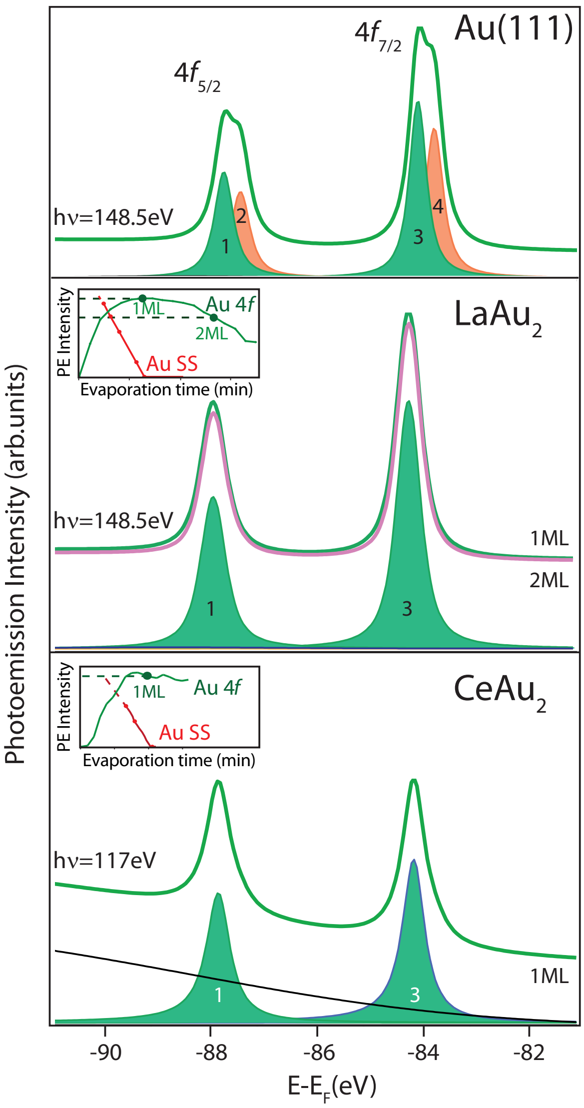

FIG. 4: $4f$ Au core-level spectra for Au(111) compared to one and two monolayers of LaAu$_2$ and one monolayer of CeAu$_2$, both grown by reactive deposition. The photon energy allows the highest surface sensitivity, as reflected in the intensity of the surface core-level shift (peaks **2** and **4**). The $4f$ component related to the surface alloy appears slightly shifted with respect to bulk Au metal (peaks **1** and **3**), although their respective emission cannot be resolved. The insets show the intensity (peak height) variation of the Shockley surface state of Au(111) (red) and the Au $4f$ alloy core-level line (green, peak **3**) across the evaporated wedges of La and Ce. The surface state quenching marks the 1 ML coverage. For Ce, the core-level intensity beyond 1 ML remains constant, indicating that multilayers are not formed under the present growth conditions.

around $\overline{\Gamma}$, whereas C disperses downwards from the center of the zone $\overline{\Gamma}$, which is reached at E$_F$. There is a sharp transition between 1ML and 2 ML in LaAu$_2$ (see Fig. 5 (b) and (c)), which involves the appearance of new bands near the Fermi level. In fact, the C band disappears and two new bands dispersing downwards appear, E and F, with energy maxima at E-E$_F$=0.44 eV and 0.77 eV. There is an additional flat band D very close to the Fermi level, which exhibits a small dispersion. An analogous transformation from 1 ML to 2 ML is also observed in GdAu$_2$ [7]. We note that bands A and C for 1 ML cross each other at 0.74 eV and k= 0.11 Å^{-1}. This point coincides with the $\overline{M}$-point of the moiré Brillouin zone (BZ). The interaction with the moiré superlattice will be analyzed in more detail through constant energy surfaces in Fig. 6. Moreover, bands A and E in the 2 ML LaAu$_2$ band structure also appear to cross each other at the same k point. p-polarized, normal emission ARPES preferentially probes states with a nodal plane parallel to the surface, and hence band crossings such as those of Fig. 5 are expected to feature hybridization gaps. However, the hybridization gap is seen in the 2 ML $A-E$ crossing of Fig. 5 (c), but it is not detected in the corresponding $A-C$ crossing of Figs. 5 (a) and (b) for 1 ML alloys.

To understand the physical nature of the ARPES bands, we perform first-principles calculations in CeAu$_2$ and LaAu$_2$ monolayer and bilayer. The calculated bands are shown in the lower pannels of Fig. 5. Here, high symmetry directions refer to the LaAu$_2$ atomic lattice. In order to make an appropriate correspondence between theory and experiment, the thickness of the bands in Fig. 5 reflects the relative weight of the orbital projection along the m=0 component of each channel. This corresponds to the largest contribution to the probability density probed in ARPES with p-polarized light and under near-normal emission. We must note the limits of the calculation, which is performed for strained alloy lattices which are forced to be commensurate with the underlying Au substrate, and also omit many-body and moiré effects. In these conditions the Fermi level (due to charge transfers) and bands (due to strain) will shift relative to one another, and relative to the substrate Au bands. We use the topological resemblance of the calculated bands with the data to identify and deduce the character of the ARPES bands.

The band labeled as B is of pure Au-d character, having a significant probability at the substrate side of the interface. Closer to E_F, the A band has La (Ce) d character with a contribution of Au p electrons from the substrate and the alloy. The C band has a dominant Au s nature, but it is also found to have a significant contribution from Au d states of substrate Au atoms, which in turn dominate in C'. The C and C' bands significantly couple to bulk Au states, explaining the slight dispersive behavior when changing the photon energy. None of these bands appear in the Au(111) bare substrate [20], and hence all are spectroscopic signatures of the LaAu$_2$ (CeAu$_2$) surface alloy.

One remarkable feature of the 2 ML LaAu$_2$ band structure in Fig. 5 (c) is the strong, flat D band emission close to E_F. The D band corresponds to a mix of Au p and La d orbitals, and is confined to the alloy. It appears unoccupied for 1 ML, and shifts below E_F in the 2 ML alloy. The analysis of the atomic orbital projections also gives some hints to understand the hybridization gap observed for A and E bands in the 2 ML, but not visible in the 1 ML A-C crossing. In the 2ML

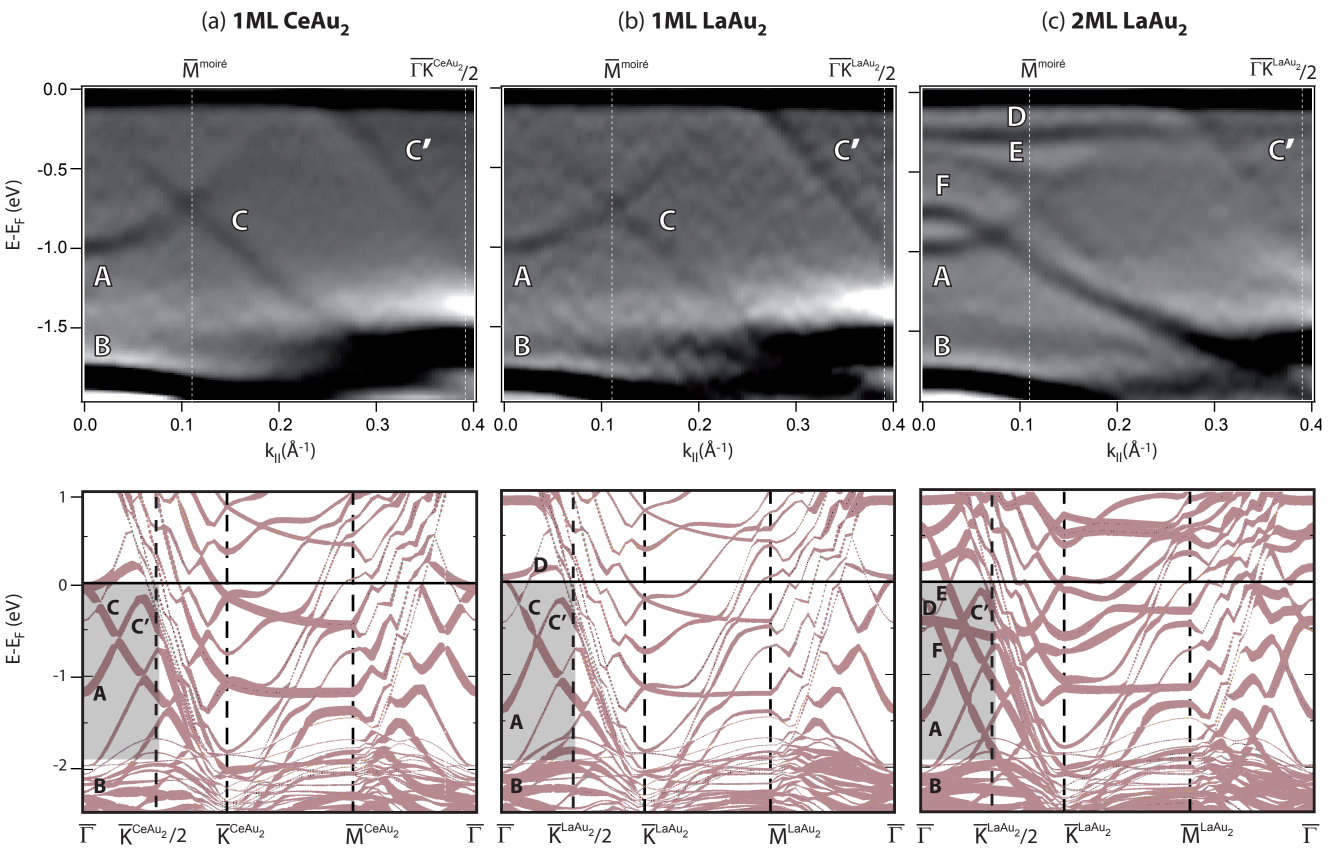

FIG. 5: Top: Two-dimensional bands measured along the $\overline{\Gamma K}$ symmetry direction for (a) 1 ML CeAu$_2$, (b) 1 ML LaAu$_2$ and (c) 2 ML LaAu$_2$ surface alloys. The different bands are labeled as in GdAu$_2$[7], due to the clear analogy among the three different lanthanide alloys. All the data correspond to the second derivative of the photoemission spectra, and have been measured with hν=44 eV for CeAu$_2$, and hν=33 eV for LaAu$_2$. The corresponding bands for GdAu$_2$ have been published elsewhere [7]. Bottom: corresponding theoretical band structures. The $\overline{\Gamma K M \Gamma}$ symmetry directions refer to those of the LaAu$_2$ 2D crystal. The width of the bands gives the relative weight of orbital projections on the m=0 channel for all angular momenta. Relative shifts (in particular for 2ML LaAu$_2$) are due to the imposition of commensurability with the substrate and the large resulting strain. The spin-up polarization is shown for the CeAu$_2$.

case the C band splits into E and F which have more weight localized in the substrate and in the ML, respectively. The F band character (Au-s in the ML) is orthogonal to A, whereas E has contributions from substrate orbitals, and interacts more strongly with A.

In Fig. 6 we further investigate the topology of the 2D band structure of 1 ML alloys through constant energy surfaces. We represent again second derivative image plots to enhance the visibility of the relatively weak features, particularly those arisen from moiré lattice scattering. In Fig. 6 (a) we show the maps for the LaAu$_2$ monolayer, whereas in panels (b)-(c) we select two characteristic surfaces for CeAu$_2$ and GdAu$_2$, measured at a photon energy of 44 eV. A, C and C' stand for the corresponding bands in Fig. 5. We have added the zone boundaries of the moiré network (in yellow) to the maps, whose periodicity can be otherwise determined from the replicas in almost all panels. Data in Fig. 6 in fact define moiré unit cells of (32±2) Å, for LaAu$_2$ and CeAu$_2$, and (35±2) Å, for GdAu$_2$, values that agree with the STM and LEED measurements, and also with previous results [7].

At the Fermi level, the dominant star-like feature corresponds to the C' band in all LaAu$_2$, CeAu$_2$ and GdAu$_2$. This is a Au d-like state, which is nominally brought to the zone center through moiré umklapps, leading to mixing with the emerging C band of Au s-character. At 0.53 eV, C adopts a hexagonal shape that is tilted 30° with respect to the moiré Wigner-Seitz hexagon. This effect reflects the 30° rotation of the atomic lattice of the alloy with respect to that of the moiré. The most interesting moiré-driven hybridization scenario occurs at 0.65 eV in Figs. 6 (a) and (b), and 0.6 eV in panel (c). At that point, A and C bands merge, leading to a A-C hybrid that is nested in the $\overline{M}$ point of the moiré BZ. Due to the 30° rotation of the hexagonally-shaped bands, such nesting leads to a triangle-like hole-pocket at $\overline{K}$, which is particularly clear for CeAu$_2$ and GdAu$_2$.

The small spectral variations among the different lanthanide alloys are better accounted for in Energy Distribution Curves (EDC) at a fixed $k_{||}$ value. EDC-s at $\overline{\Gamma}$ for the whole series of 1 ML and 2 ML alloys are shown in Fig. 7. Energies for the different transitions are summarized in Table I. C is

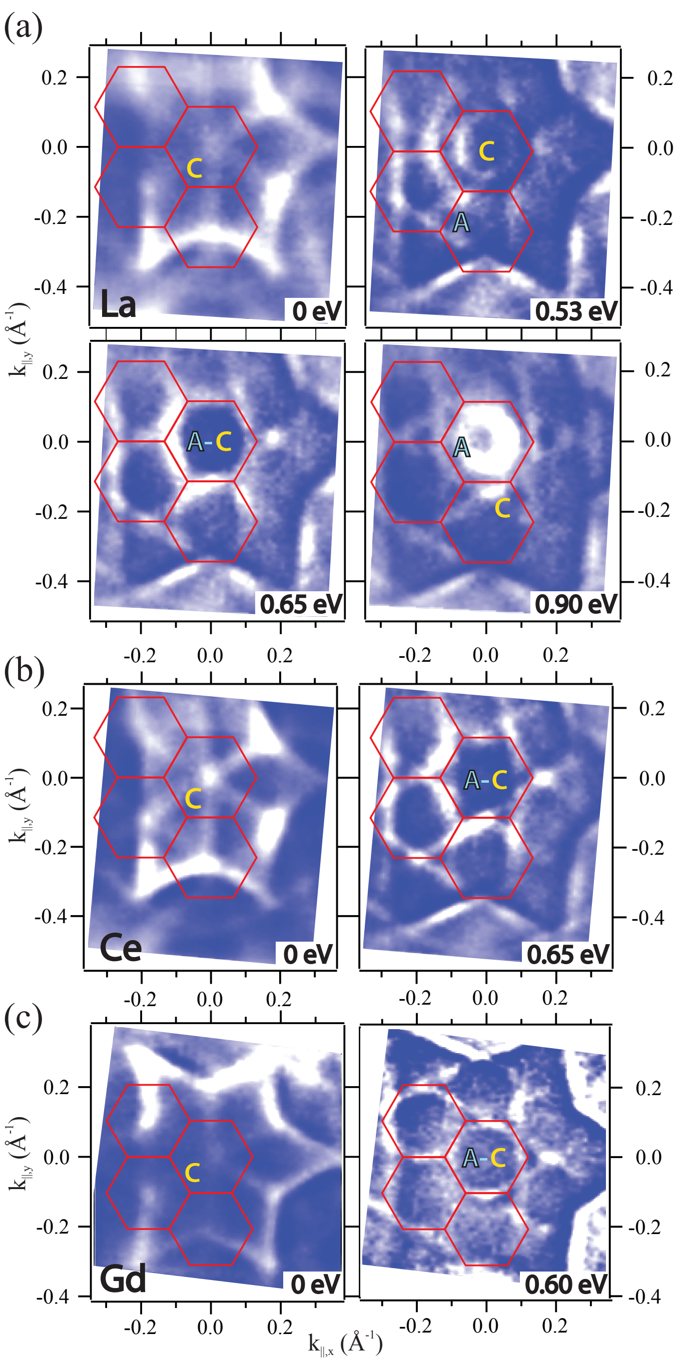

FIG. 6: Constant energy surfaces at various energies for (a) 1 ML $LaAu_2$, (b) $CeAu_2$, and (c) $GdAu_2$, all measured with hν=44 eV. Maps correspond to the second derivative of the photoemission intensity. The BZ of the moiré is drawn with yellow hexagons and the labeling corresponds to bands in Fig. 5. Features appear replicated due to the moiré superlattice. At the Fermi level, the dominant intensity corresponds to C' band, which is brought to the zone center through moiré umklapps. At -0.65 eV in panel (a) and (b) and at -0.6 eV in panel (c), A and C merge into a single moiré-nested band.

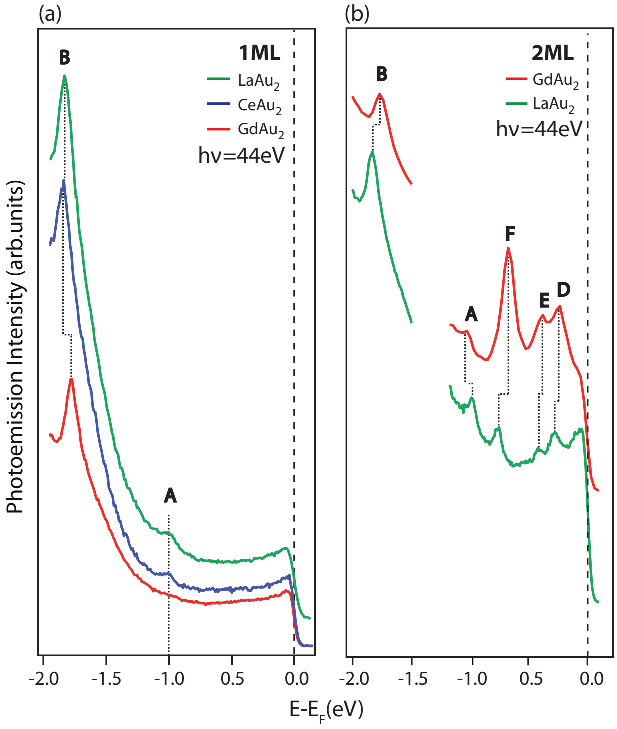

FIG. 7: Energy Distribution Curves for (a) 1 ML and (b) 2 ML, as measured at $\overline{\Gamma}$ ($k_{||}$=0 for the different $ReAu_2$ surface alloys, including $GdAu_2$ from Ref. [6]. The indicated photon energies are selected to enhance the peak intensities in each case. Peak energies are listed in Table I.

absent in these EDC-s, since it crosses $\overline{\Gamma}$ at E_F. Thus, with the aim of including C in the comparative analysis, in table I we include its Fermi velocity, measured at similar photon energies for the three alloys. Lanthanide d-like A band has its minimum binding energy at 1.02 eV for $LaAu_2$, although it shifts only 20 meV from La to Ce or Gd and from 1 ML to 2 ML, i.e., a small variation that falls within the experimental accuracy. Also for the Fermi velocity of C, values around $0.8{\cdot}10^6$ m/s are found in all cases. In contrast to these similarities, the Au d-like B band, as well as D, E and F bands in 2 ML alloys, exhibit a larger variation of 50-80 meV from Gd to La. For 1 ML alloys, there are no major differences among the lanthanides (Fig. 7 (a)). In contrast, for 2 ML of $GdAu_2$ and $LaAu_2$, we note that A, which has a larger probability on lanthanide atoms, shifts in the opposite direction than B, D, E, and F, which have more weight in Au atoms. Therefore, the shift in Fig. 7 (b) is probably of chemical nature, i.e., it depends on the type of lanthanide that makes up the surface alloy.

SUMMARY

We have investigated the structure and electronic properties of two novel surface alloys, $LaAu_2$ and $CeAu_2$, comparing them with the already studied $GdAu_2$ case [6, 7]. By STM we observe a complete structural analogy ($REAu_2$), with similar moiré and atomic lattice periodicities that vary slightly

	Coverage	**A (eV)**	**B(eV)**	**D(eV)**	**E(eV)**	**F(eV)**	**C (v_F(m/s))**
La	1ML	-1.02	-1.84				$0.85{\cdot}10^6$
La	2ML	-1.02	-1.84	-0.30	-0.44	-0.77	
Ce	1ML	-1.00	-1.83				$0.80{\cdot}10^6$
Gd	1ML		-1.78				$0.74{\cdot}10^6$
Gd	2ML	-1.04	-1.77	-0.24	-0.39	-0.69	

TABLE I: Two-dimensional electronic band energies at $\overline{\Gamma}$ ($k_{\|}$=0) for 1 and 2 ML $REAu_2$ alloys, as measured with 44 eV photon energy and with respect to E_F. Labels refer to the distinct bands in Fig. 5. The C band energy is zero, since it crosses E_F at $\overline{\Gamma}$ in all cases. For the latter, we show the Fermi velocity measured at E_F with hν=44 eV.

depending on the lanthanide atoms. The electronic structure has been analyzed by ARPES through two-dimensional band dispersion, constant energy surfaces, and energy distribution curves spectra, also offering an overall resemblance over the different alloys. The physical-chemical nature of each electronic band has been clarified by direct comparison with first-principles calculations performed for mono and bilayers. Beyond the pure identification of the measured bands, the calculation has allowed us to understand the nature of electronic states that mix through scattering with the moiré superlattice.

This work was supported in part by the Spanish MICINN (MAT2010-21156-C03-01 and -C03-03) and the Basque Government (IT-621-13). The SRC is supported by the NSF under Grant No. DMR-0537588. The authors acknowledge an A.R.C. grant (TheMoTherm 10/15-03) from the CfBelgique. Computer time was made available by PRACE-2IP DECI-8 (EU FP7 grant RI-283493) and the Belgian CECI.

---

[1] C. J. Baddeley, M. Tikhov, C. Hardacre, J. R. Lomas, and R. M. Lambert, "Ensemble effects in the coupling of acetylene to benzene on a bimetallic surface: A study with pd111/au," *The Journal of Physical Chemistry*, vol. 100, no. 6, pp. 2189–2194, 1996.

[2] L. Fernández, M. Corso, F. Schiller, M. Ilyn, M. Holder, and J. E. Ortega, "Self-organized growth of high density magnetic co nanodot arrays on a moiré template," *Applied Physics Letters*, vol. 96, no. 1, p. 013107, 2010.

[3] H. Brune, M. Giovannini, K. Bromann, and K. Kern, "Self-organized growth of nanostructure arrays on strain-relief patterns," *Nature*, vol. 394, no. 6692, pp. 451–453, 1998.

[4] N. Nilius, E. D. L. Rienks, H. Rust, and H. J. Freund, "Self-organization of gold atoms on a polar feo(111) surface," *Phys. Rev. Lett.*, vol. 95, p. 066101, Aug 2005.

[5] A. T. N'Diaye, S. Bleikamp, P. J. Feibelman, and T. Michely, "Two-dimensional ir cluster lattice on a graphene moiré on ir(111)," *Phys. Rev. Lett.*, vol. 97, p. 215501, Nov 2006.

[6] M. Corso, M. J. Verstraete, F. Schiller, M. Ormaza, L. Fernández, T. Greber, M. Torrent, A. Rubio, and J. E. Ortega, "Rare-earth surface alloying: A new phase for gdau$_2$," *Phys. Rev. Lett.*, vol. 105, p. 016101, Jul 2010.

[7] M. Corso, L. Fernndez, F. Schiller, and J. E. Ortega, "Au(111)-based nanotemplates by gd alloying," *ACS Nano*, vol. 4, no. 3, pp. 1603–1611, 2010. PMID: 20146459.

[8] L. Fernández, M. Blanco-Rey, M. Illyn, L. Vitali, A. Correa, P. Ohresser, J. Ortega, A. Ayuela, and F. Schiller. *Unpublished.*

[9] D. Givord, "Introduction to magnetism and magnetic materials," *Lecture notes in Physics: Magnetism and Synchrotron radiation*, vol. 565, pp. 3–23, 2001.

[10] I. D. Hughes, M. Dane, A. Ernst, W. Hergert, M. Luders, J. Poulter, J. B. Staunton, A. Svane, Z. Szotek, and W. M. Temmerman, "Lanthanide contraction and magnetism in the heavy rare earth elements," *Nature*, vol. 446, no. 7136, pp. 650–653, 2007.

[11] Z. Fisk, D. W. Hess, C. J. Pethick, D. Pines, J. L. Smith, J. D. Thompson, and J. O. Willis, "Heavy-electron metals: New highly correlated states of matter," *Science*, vol. 239, no. 4835, pp. 33–42, 1988.

[12] J. Li, W. D. Schneider, R. Berndt, and B. Delley, "Kondo scattering observed at a single magnetic impurity," *Phys. Rev. Lett.*, vol. 80, pp. 2893–2896, Mar 1998.

[13] F. Patthey, J.-M. Imer, W.-D. Schneider, H. Beck, Y. Baer, and B. Delley, "High-resolution photoemission study of the low-energy excitations in 4*f* electron systems," *Phys. Rev. B*, vol. 42, pp. 8864–8881, Nov 1990.

[14] A. C. Hewson, *The Kondo problem to heavy fermions*. Cambridge University Press, 1993.

[15] P. M. A. J. M. B. X. Gonze, B. Amadon *et al.*, "Abinit: First-principles approach to material and nanosystem properties," *Comput. Phys. Commun.*, vol. 180, pp. 2582–2615, 2009.

[16] P. E. Blöchl, "Projector augmented-wave method," *Phys. Rev. B*, vol. 50, pp. 17953–17979, Dec 1994.

[17] V. I. Anisimov, J. Zaanen, and O. K. Andersen, "Band theory and mott insulators: Hubbard U instead of stoner I," *Phys. Rev. B*, vol. 44, pp. 943–954, Jul 1991.

[18] S. Ma, X. Zhao, J. A. Rodriguez, and J. Hrbek, "Stm and xps study of growth of ce on au(111)," *The Journal of Physical Chemistry C*, vol. 111, no. 9, pp. 3685–3691, 2007.

[19] The band structure is measured 5 degrees off the ΓK high symmetry direction. The Fermi mappings in Fig.6 indicate that this small rotation angle has minor effects on the band structure compared to the one observed along the ΓK direction.

[20] C. B. Sommers and H. Amar, "Relativistic band structure of gold," *Phys. Rev.*, vol. 188, pp. 1117–1120, Dec 1969.